



Seismic imaging east of the Rocky Mountains with USArray



Robert W. Porritt^{a,*}, Richard M. Allen^a, Fred F. Pollitz^b

^a Department of Earth and Planetary Sciences, University of California, Berkeley, United States

^b USGS, Menlo Park, United States

ARTICLE INFO

Article history:

Accepted 23 October 2013

Available online 11 November 2013

Editor: P. Shearer

Keywords:

seismology

geophysics

Wyoming Province

Llano Province

Deep Farallon slab

ABSTRACT

USArray has facilitated significant advancement in tomographic models and methodologies. While there persists a fundamental tradeoff between horizontal and vertical resolution due to the components of the wave train analyzed, advances in joint inversions are continuing to refine the tomographic images generated with USArray. The DNA13 model incorporates teleseismic P observations, independent SH and SV observations, and surface-wave phase velocities from both teleseismic earthquakes and ambient noise to constrain the relative wave-speed from the crust down into the lower mantle. We address the validity of our models through forward prediction of observables and compare the predictive power of the DNA13 models to other models. In the shallow portion of DNA13, we image the Archean age Wyoming Province, which exhibits evidence of ocean closure at its northern and southern ends. The Llano Province in Central Texas is of Grenville age and still contains lithospheric evidence of subduction as the province accreted to North America. Comparison of these two provinces highlights the role of fossil slabs as part of the cratonic architecture. Analysis of the deep portion of the models highlights variations within the Farallon plate, including two distinct high wave-speed anomalies in the eastern U.S. and a shallow feature in the center of these two anomalies. We propose this is evidence of an oceanic plateau, which provides the necessary positive buoyancy to promote flat-slab subduction of the Farallon plate.

Published by Elsevier B.V.

1. Introduction

The ability to map the internal velocity structure of the Earth is rapidly advancing due to the seismic waveform dataset provided by USArray. Prior to the array (with a ~ 70 km station spacing) rolling across the U.S., global models showed a clear contrast between the deformational western U.S. from the stable cratonic eastern U.S. in the upper 200 km (van der Lee and Nolet, 1997). In the lower mantle, the relatively cold Farallon slab is visible below the transition zone in the eastern U.S., contrasting with the warm to neutral mantle under the western U.S. (Grand, 1994; van der Hilst et al., 1997). Body-wave tomography models utilizing USArray are now recovering high-resolution images revealing dynamic interactions between high velocity anomalies, interpreted as slabs and drips, and low velocity features such as the Yellowstone Plume and the Rio Grande Rift (Burdick et al., 2008; Obrebski et al., 2010, 2011; Xue and Allen, 2010; Schmandt and Humphreys, 2010; James et al., 2011; Sigloch, 2011; Tian et al., 2011; Becker, 2012; Pavlis et al., 2012). Now that USArray is crossing the Midwest U.S. and approaching the east coast, the picture that is emerging begins

to contain elements of both the high-resolution body-wave models and the longer wavelength global models.

One prominent province recently resolved by USArray is the Archean age Wyoming Province (Fig. 1) (Roscoe and Card, 1993; Ross, 2002; Foster et al., 2006; Whitmeyer and Karlstrom, 2007). This province is one of a handful of Archean provinces forming the core of the Laurentia Craton after assembly in the Trans-Hudson Orogen during the Paleoproterozoic between 1.85–1.78 Ga (Hoffman, 1988; Whitmeyer and Karlstrom, 2007). The Little Belt Arc is at the northern boundary of the Wyoming Province (Whitmeyer and Karlstrom, 2007), linking it with the Archean Medicine Hat Block (Villeneuve et al., 1993; Mueller et al., 2002) and the Trans-Hudson Orogen is at the eastern boundary with the Superior Province (Frederiksen et al., 2007). Its southern margin is the Cheyenne Belt where northward thrusting at amphibolite facies followed by strike-slip motion at Greenschist facies suggests an accretionary collision (Duebendorfer and Houston, 1986). Imaging in the CD-ROM experiment by Yuan and Dueker (2005) suggests a slab associated with this event (the Cheyenne Slab) is still visible under the Cheyenne Belt.

Following the accretion of the Wyoming Province, a series of orogens grew the continent from the south–southeast starting with the Yavapai (1.8–1.7 Ga), then the Mazatzal (1.7–1.6 Ga), and finally the Grenville (1.3–1.0 Ga). Plutons associated with these orogens helped weld together the young continent and allow precise age dating. During the Grenville orogeny, the last major continental

* Corresponding author. Tel.: +1 906 281 3675.

E-mail address: rob@seismo.berkeley.edu (R.W. Porritt).

¹ Currently at Department of Earth Science, University of Southern California.

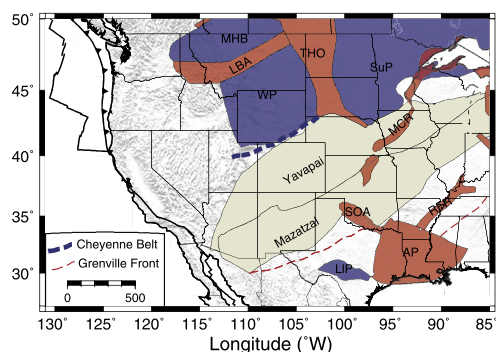


Fig. 1. Location map highlighting provinces east of the Rocky Mountains. The background is a shaded relief map. Colored polygons display cratonic pieces in purple and orogens and rifts in red. Polygons and names from [Whitmeyer and Karlstrom \(2007\)](#) include the Medicine Hat block (MHB), Little Belt Arc (LBA), Trans-Hudson Orogen (THO), Superior Province (SuP), Wyoming Province (WP), Keweenaw Mid-Continent Rift (MCR), Southern Oklahoma Aulacogen (SOA), Reelfoot Rift (RFR), Argentine Precordillera (AP), and Llano Province (LIP). Yavapai and Mazatzal provinces are shaded beige. Dashed lines denote the Cheyenne Belt and the Grenville Front. (For interpretation of the references to color in this figure legend, the reader is referred to the web version of this article.)

component of the Precambrian craton, the Llano province, formed a distinct sequence associated with back-arc rifting, crustal formation, and ocean closure through northward-directed subduction ([Mosher, 1998](#)). Major rifting events also contribute to the mosaic of Laurentia, including the ~ 1.1 Ga Keweenaw Mid-Continent Rift ([Van Schmus and Hinze, 1985](#)) and the ~ 515 Ma Cambrian Southern Oklahoma Alucogen ([Keller and Stephenson, 2007](#)), Reelfoot Rift ([Braile et al., 1986](#)), and break-off of the Argentine Precordillera ([Thomas and Astini, 1999](#)).

The late Mesozoic and Cenozoic tectonism is largely controlled by eastward progressing subduction of the Farallon plate ([Schellart et al., 2010](#)). The Juan de Fuca, Gorda, and Monterey ([Wang et al., 2013](#)) plates are the young western remnants of the Farallon observable off the U.S. west coast. The long history (>150 Ma) of this plate has contributed to significant tectonic uplift and magmatism throughout the western U.S. The inboard uplift of the Rocky Mountains and magmatic hiatus from 90–30 Ma followed by the ignimbrite flare-up indicates the slab became flat during this period ([Humphreys et al., 2003](#)). The mechanism by which the flat-slab episode initiated is unclear, but modeling work by [Liu et al. \(2010\)](#) suggests that subduction of two oceanic plateaus may have provided the necessary buoyancy due to the thick crustal layers. These plateaus are conjugates to the Hess Rise and Shatsky Rise in the Pacific Ocean and the geodynamic model of [Liu et al. \(2010\)](#) puts them between 900 km and 1500 km below eastern North America.

In this study we present the new tomographic model, DNA13. This model contains four independent estimates of the isotropic velocity structure useful for imaging relative mantle thermal and compositional anomalies. We address the validity of the model through an assessment of its predictive power against a synthetic waveform dataset computed for a 3D global model. We then use DNA13 to compare and contrast the Archean Wyoming craton and the Mesoproterozoic Llano province. Below the mantle transition zone, the Farallon slab is observed to have significant topography and two isolated high velocity anomalies. We propose these high velocity anomalies are either the result of a subducted ridge-plume interaction or the subducted oceanic plateaus modeled by [Liu et al. \(2010\)](#) and that the topography of the slab suggests unmodeled complexity associated with subducted heterogeneities.

2. Method

The DNA13 models are constructed in a similar manner as DNA09 ([Obrebski et al., 2010](#)) and DNA10 ([Obrebski et al., 2011](#)), but with some significant updates. For the body-wave portion of DNA13, the instrument corrected ground velocity is rotated from the vertical, east, and north coordinate frame into the P–SV–SH coordinate frame utilizing the slowness parameter computed for the IASP91 ([Kennett and Engdahl, 1991](#)) model via the TauP toolkit ([Crotwell et al., 1999](#)). Arrival time windows are picked for the direct P, SV, and SH arrivals and the relative delay times are refined with the [VanDecar and Crosson \(1990\)](#) multi-channel cross-correlation method in period bands determined by the dominant period for the phase after visual inspection of the arrivals. The P-velocity model uses the 1.25–2.5 s period band, while the SV and SH models use the 10–50 s band. Arrivals are only accepted if they have a minimum correlation coefficient of 0.9 (see Table S1 for number of events and observations accepted per model). The station and event coverage of the P model is shown in [Fig. 2](#) and the coverage of the S models is shown in [Fig. S1](#). The sensitivities of the band-limited delays are computed with the finite frequency kernels of [Hung et al. \(2000\)](#) and the body-wave models are computed via an LSQR inverse problem solver.

In addition to the P, SV, and SH body-wave-only models, the joint body-wave–surface-wave inversion method of [Obrebski et al. \(2011\)](#) is used to invert Rayleigh Wave phase velocities with the SV body-wave delay times to form the DNA13-SV-Joint model. This includes constraints from an updated dataset of phase velocities from [Pollitz and Snoko \(2010\)](#), who use local fits to teleseismic earthquakes, and also an expanded dataset from [Porritt et al. \(2011\)](#), who uses ambient seismic noise to estimate phase velocities across the study region. Together, these two datasets span the 8–125 s period band and provide regularly sampled phase velocity maps. Previous studies (e.g. [Yang et al., 2008](#)) have shown

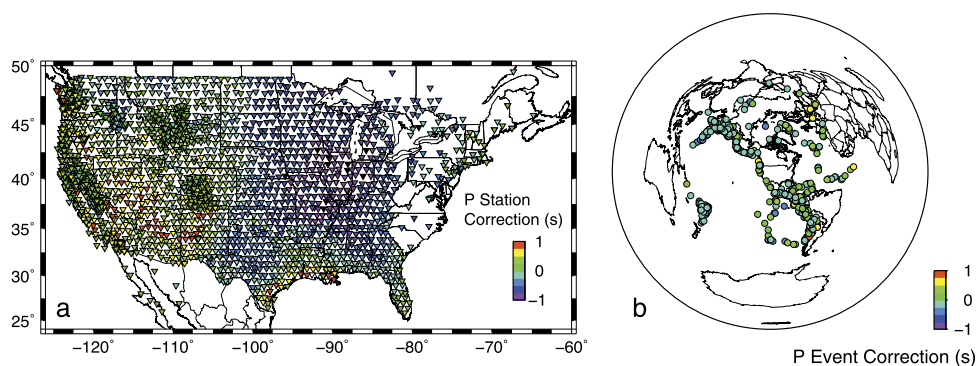


Fig. 2. Station correction (a) and event correction (b) terms for DNA13-P. All color scales given in seconds. (For interpretation of the references to color in this figure legend, the reader is referred to the web version of this article.)

the two types of datasets are consistent with each other and visual assessment of sample dispersion curves has found the two measurements are within uncertainty of each other where they overlap. To combine the datasets, both are used where they overlap, but with greater weight given to the ambient noise dataset at the shorter periods and greater weight given to the teleseismic derived dataset at the longer periods via the weighting factor q shown in the top panel of Fig. S2. This is done to account for variability in the seismic source because ambient seismic noise is strongly excited in the shorter periods (8–40 s) whereas teleseismic earthquakes excite longer period waves (30–125 s).

The models are inverted for relative velocity perturbation on static grids without adaptive refinement. The body-wave-only models have sufficient coverage from 126°W to 72°W and 25°N to 52°N with node spacing of 0.42° in both lateral directions and 20 km in depth. The surface-wave dataset is less extensive laterally due to the requirement of longer duration measurements at station sub-arrays (see Fig. S3), but the improved vertical resolution allows the vertical spacing to be reduced to 10 km for the SV-Joint model. The grid for the SV-Joint model is defined from 126°W to 90°W, 25°N to 52°N with spacing of 0.6° longitude by 0.45° latitude. The bottoms of all the models are constrained to 1280 km depth as we expect sub-transition zone anomalies to be relatively minor and crossing raypaths at greater depths are limited.

In the damped LSQR inverse solution for the models, we also solve for static station and event corrections. The station corrections account for shallow short-wavelength, and therefore unresolvable structure, beneath the stations; the event corrections accommodate errors in the timing and location of events as well as common structure out of the model space. In order to solve for the SV-Joint inversion we first convert the phase velocity observations to perturbations to the 1D WUS model of [Pollitz and Snoke \(2010\)](#) with a correction for the crustal thickness from [Chulick and Mooney \(2002\)](#). Second, a weighting parameter, p , must be determined for the relative weight of the body-wave delays versus the phase velocity perturbations ([Julia et al., 2000](#)) for the joint inversion matrix. We use a weight of 0.7 based on the trade-off analysis of [Obrebski et al. \(2011\)](#). Finally, a linear ramp in the sensitivity of the travel time delays to the velocity structure in the upper 60 km is imposed with zero weight at the surface and a weight of 1 at 60 km depth to reduce the influence of the body waves on shallow velocity structure where the rays do not cross and provide little sensitivity. The remaining short-wavelength structure in the body-wave delays is absorbed with station corrections as with the body-wave-only models.

3. Resolution

The surface-wave inversion is a two-step procedure, and thus resolution must be addressed at both steps. The resolution of the ambient noise alone is shown in Fig. S3. This is a resolution estimate from the method of [Barmin et al. \(2001\)](#), which approximates the resolvable wavelength of a delta function as a spatial map. This is shown at two periods representing the shorter periods well recovered by ambient noise and the longer periods less well recovered by noise alone.

The resolution of the body-wave models and the SV-Joint model is determined through the standard checkerboard resolution test. Progressively smaller checkers are employed to determine the range of recoverable anomaly wavelengths. Fig. S4 illustrates the checkerboard resolution of the P, SH, and SV body-wave-only models and Fig. S5 displays the SV-Joint model. The tests show slightly better recovery of the P model relative to the SH model at 200 km (note the different cell sizes that are being recovered in Fig. S4), likely due to the narrower sensitivity kernel of the higher fre-

quency P-waves. It is also notable that the P-wave model at 200 km shows better amplitude recovery around Yellowstone and southern California due to the increased station coverage of these regions. The deeper portions of the model require larger checkers for acceptable recovery, and all the features interpreted below are the size of these recovered blocks or larger.

The SV-Joint model has similar recovery to the SV model in the transition zone, but the shallow recovery (<200 km) is much improved due to the inclusion of surface waves. The improved recovery of the SV-Joint model is illustrated in Fig. S6. The checkers are the same size in each row, but with the SV model in the left panels and SV-Joint model in the right column. The small checkers in the shallow cross-section (Fig. S6a, f) are well recovered by the SV-Joint model, but are vertically elongated in the SV body-wave-only model. At greater depths, with larger checkers (Fig. S6d, e, i, j), the recovery is identical between the two models.

4. Validation test

An important aspect of seismological models is the ability to predict independent observations. Checkerboard tests are able to assess the resolving power of the inversion matrix, but they are unable to address the accuracy of the input data. Alternatively, construction of full waveform synthetics based on the tomographic model is sometimes used for validation, but these methods are limited by computational cost and are unable to recover high frequency arrivals. Therefore, we determine the predictive power of the model by measuring the arrival times of a set of teleseismic events not used in DNA13 and comparing those measurements with the expected arrival times based on DNA13. We present the results as probability density functions in Fig. S7 and summarize with the correlation coefficient, R . The probability density functions display the relative probability of occurrence between observed and predicted delays. A correlation coefficient of 1 indicates a linear relationship such that the observed delays are perfectly predicted by the model and a coefficient of 0 means there is no relationship between observed and predicted delays.

We perform the test for three different datasets. First, we compare the data used in the inversion to delay times predicted by the model (Fig. S7a–d). We calculate these delay times by solving the forward problem using the finite frequency sensitivity matrix and the velocity model. This provides an estimate of the expected data fit. We next compare the observed and predicted delays for a set of events not used in the inversion. As shown by the probability density functions and correlation coefficients (Fig. S7e–h), these predicted delay times are fit nearly as well as the data used in the inversion. This suggests these delays are well predicted by the DNA13 model. Finally, we measure arrival times from synthetic waveforms computed with the Spectral Element Method through the 3D Global model S362ANI and CRUST2.0 ([Tromp et al., 2010](#)). These synthetics are now available through IRIS for a limited set of events. The fit of this model is not as good as DNA13, but still shows a positive correlation indicating a moderate fit.

5. Results

5.1. Comparison with previous models

The proliferation of USArray based models ([Becker, 2012](#); [Pavlis, 2011](#)) provides an opportunity to compare DNA13 with broader scale surface-wave models and recent work synthesizing observations of multiple USArray models. We compare DNA13-SH with the SH model from [Yuan et al. \(2011\)](#) and the SMEAN-WUS model of [Becker \(2012\)](#) (Fig. 3) as they are similarly defined shear velocity models. The SAWum_NA2 of [Yuan et al. \(2011\)](#) incorporates USArray data, but the recovered structure is much longer wavelength than both the SMEAN-WUS model and DNA13-SH due to

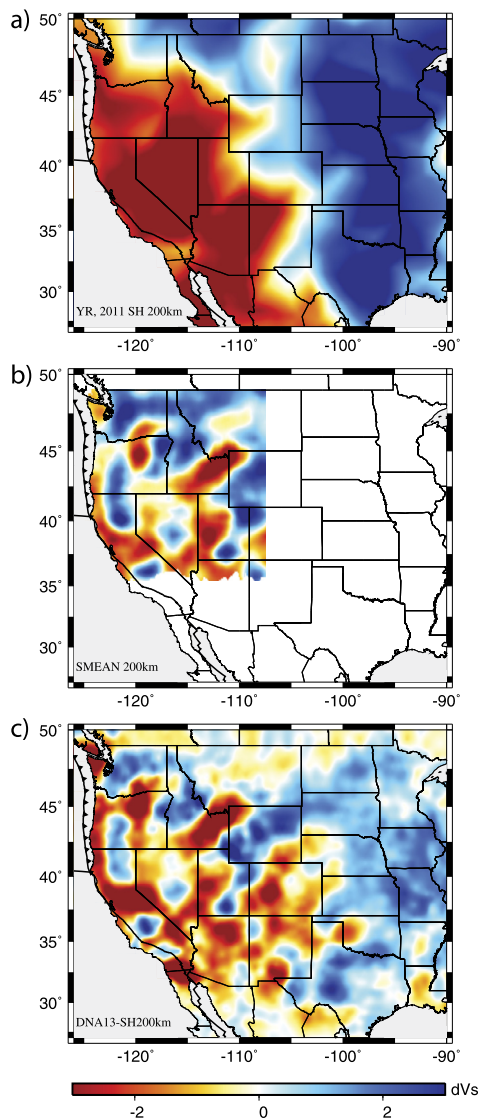


Fig. 3. Comparison of DNA13-SH with other recent models. Panel (a) is the SH model of Yuan et al. (2011), panel (b) is the western US smean model from Becker (2012) computed by averaging three recent S-wave models from USArray, and panel (c) is DNA13-SH with up-scaled amplitudes following Becker (2012). All maps are plotted on the same scale with a common color bar representing the velocity perturbation to a 1D mean at 200 km depth. (For interpretation of the references to color in this figure legend, the reader is referred to the web version of this article.)

its dataset of long period surface waves and SKS waves. At the scale of DNA13, the observable structure is limited to only east–west contrast between the craton and the cordillera. Some shorter wavelength information is visible in SAWum_NA2 at the transition from craton to cordillera, but this information is more clearly seen in the body-wave derived SMEAN-WUS and DNA13. The SMEAN-WUS model is not as extensive laterally as the two other models due to being limited by the smallest model used in the averaging, but it shows significant variation in the cordillera structure. DNA13-SH has similar structure in the cordillera to SMEAN-WUS, but the greater lateral extent of the DNA13 illustrates the east–west contrast also seen in the SAWum_NA2 model.

5.2. Upper 200 km structures

The upper 200 km of the model encompasses the crust, thin Phanerozoic lithosphere, most of the cratonic lithosphere, and a portion of the western U.S. asthenosphere and is best represented

by the SV-Joint model (Fig. 4). There is marked contrast between the slow western U.S. and fast eastern U.S. throughout the upper 200 km. The shallowest map displayed, at 25 km, depicts mostly mid to lower crustal structure with pockets of upper mantle lithosphere in central California (CC) and the California–Arizona (SC) border. The crust east of the Rocky Mountain Front (RMF) is largely high velocity, with the notable low velocity crescent along the Gulf Coast (GC) of Texas and Louisiana. High velocities in the western U.S. crust are primarily located in the Colorado Plateau (CP) and Columbia River Basalts (CRB) regions.

At sub-crustal depths, three high velocity features begin to emerge in the cordillera. First, the Juan de Fuca slab (JdF) is a north–south oriented high velocity feature most noticeable below 100 km depth. This slab is only slightly high velocity, which may be due to a relatively weak contrast with the lower cratonic lithosphere to the east. The second high velocity feature we note is the Colorado Plateau. In this region, the central high velocity of the lower crust disappears in the upper lithosphere and is replaced by two high velocity bodies at the northwest and southeast edges. These features have previously been interpreted as lithospheric drips (Sine et al., 2008; Obrebski et al., 2011; Liu et al., 2011) and this model is consistent with that interpretation. The last features we note here are the Isabella Anomaly (IA) (Zandt et al., 2004; Frassetto et al., 2011) and Transverse Ranges Anomaly (TR) (Nicholson et al., 1994) in southern California. These high velocity bodies are in a region of slightly thicker crust than the surrounding and have been argued to be either a plate fragment or a lithospheric instability (Zandt et al., 2004; Frassetto et al., 2011; Wang et al., 2013; Pikser et al., 2012).

Low velocities are mostly observed in the western U.S. and a few of these are exceptionally high amplitude slow features. The Yellowstone (YS) hotspot is observed as very low velocity at the northeast end of the Snake River Plain (SRP) throughout the upper 200 km (Waite et al., 2006; Xue and Allen, 2007; James et al., 2011; Obrebski et al., 2011; Schmandt et al., 2012). At 200 km, the slab window is visible as a low velocity anomaly between the southern edge of the JdF and the northern edge of the IA (Liu et al., 2012). Other low velocity features tend to focus along province boundaries such as around the Colorado Plateau and eastern Sierra Nevada (Obrebski et al., 2011). One other notable feature from 75–200 km depths is a gradational west to east increase in velocity towards the center of the Laurentia craton (LC). This may reflect the increasing lithospheric thickness across the transition from cordillera to craton.

5.3. Deeper structures

The three body-wave components of DNA13 show largely consistent structure in the sub-lithospheric mantle (Fig. 5). The broad east–west contrast between the low velocity west and high velocity east is seen at both 200 km and 600 km depths. In the eastern U.S. at 600 km, two unusually high velocity anomalies (F1 and F2) are observed in all three models and under the Llano Province (LI) there is a west–northwest to east–southeast oriented high velocity anomaly. Yellowstone, in the northwestern part of the model, is consistently low velocity at 200 km and 600 km depths in all three models. Regions of notable difference between the three models include the JdF slab and the Nevada Anomaly (NA) in the 200 km depth map. The JdF in the P and SH models is largely continuous with a low velocity hole at the Washington–Oregon border, whereas the SV model is less continuous. The high velocity of the NA is seen in the P model to extend from the center of Nevada northeast to immediately south of Yellowstone, but the SH and SV models are limited to a circular region in the center of Nevada. While this suggests a possible region of heightened Vp/Vs ratio, the lack of a well-defined background model makes interpretation

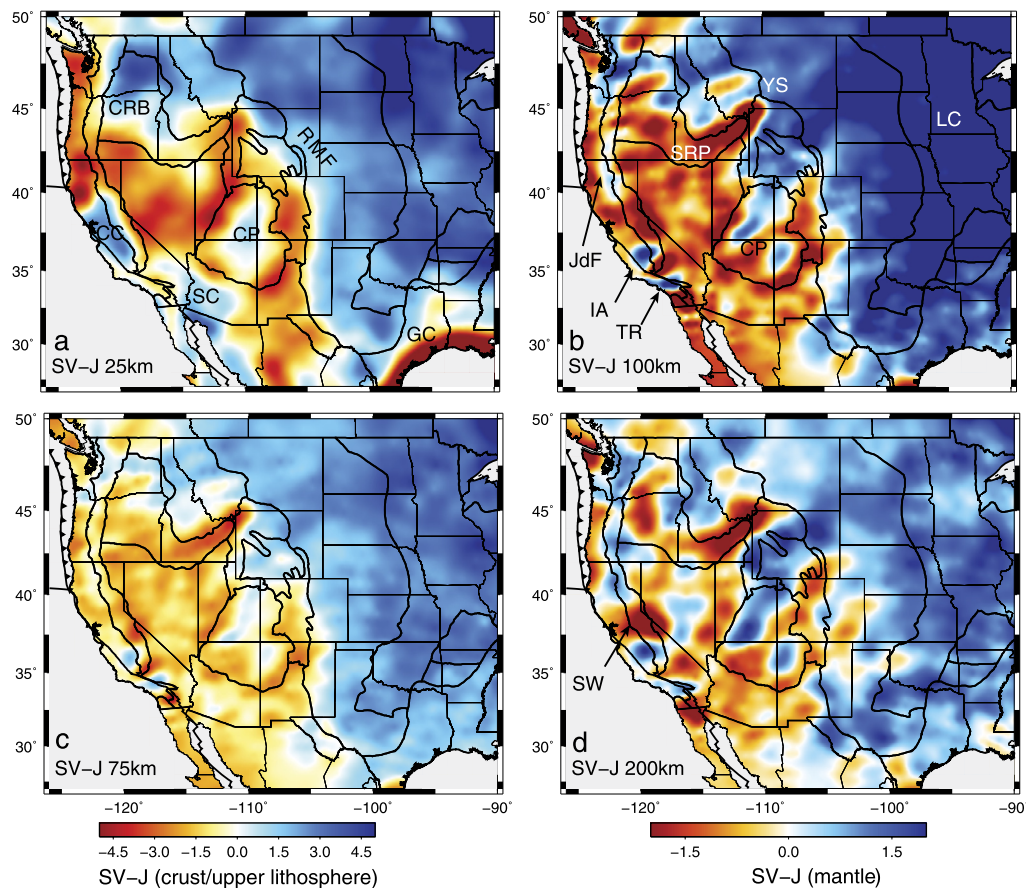


Fig. 4. Shallow structure for the SV-Joint model. Depths for (a–d) given in lower left-hand corner. Physiographic provinces of [Fenneman and Johnson \(1946\)](#) are overlain in black. Annotations are given for the Rocky Mountain Front (RMF), Columbia River Basalts (CRB), Central California (CC), Southern California (SC), Colorado Plateau (CP), Gulf Coast (GC), Juan de Fuca Slab (JdF), Isabella Anomaly (IA), Transverse Range Anomaly (TR), Yellowstone (YS), Snake River Plain (SRP), Slab Window (SW), and Laurentia Craton (LC).

of this feature tenuous. At 600 km depth, the SV model is dissimilar to the other models south of Yellowstone where the P and SH models show a continuous east–west high velocity anomaly from the coast to the craton, but the SV high velocity is more limited spatially.

6. Discussion

The progression of USArray through the Laurentia Craton is providing detailed images of the remnants of continental creation. The Archean age Wyoming Province and Mesoproterozoic Llano Province represent the early (~ 1.8 – 2.0 Ga) and late (~ 1.3 – 1.0 Ga) stages of continental accumulation. The proposed primary mechanisms of continental lithosphere formation are stacking of oceanic slabs and amalgamation of volcanic arcs ([Lee, 2006](#)). Of these two mechanisms, seismic imaging has proven most useful at identifying slabs layered along the base of the lithosphere as they appear to either have a strong impedance contrast (e.g. [Bostock, 1998](#)), changes in anisotropy (e.g. [Snyder, 2008](#)), or are a dipping high velocity body (e.g. [Yuan and Dueker, 2005](#)).

The deep structure of the model is primarily associated with the subducting Farallon plate. Fragments of this plate can be traced from the eastern U.S. to the modern Juan de Fuca system ([Sigloch, 2011](#); [Pavlis, 2011](#); [Burdick et al., 2012](#)). Detailed imaging of this slab has proven difficult because a thick high velocity cratonic lid ([Abt et al., 2010](#)) over a high velocity slab is difficult to image with body waves alone due to the near vertical ray propagation. Our joint body-wave–surface-wave inversion overcomes this limitation by partitioning the proper amount of high velocity anomaly

to the near surface and thereby allowing improved imaging of high velocity in the sub-lithospheric mantle.

6.1. Wyoming Province

The Archean age (>2.5 Ga) Wyoming Province (WP) is depicted in [Fig. 6](#). The map views of the model ([Fig. 6a,b](#)) show high velocities for the WP are contiguous with the Laurentia Craton. The lithospheric map, at 100 km depth, shows two significant low wave-speed anomalies associated with the Little Belt Arc ([Whitmeyer and Karlstrom, 2007](#)) and the Yellowstone Plume ([Waite et al., 2006](#); [Xue and Allen, 2007](#); [Obrebski et al., 2011](#); [Schmandt et al., 2012](#)). The Little Belt Arc is at the periphery of the province, but the Yellowstone plume intrudes on the province as a low shear velocity anomaly of -3% . Cross-section A–A' ([Fig. 6c](#)) shows that the low velocity anomaly beneath Yellowstone is contiguous to the bottom of the model, but with significant deflection through the transition zone ([Schmandt et al., 2012](#)). [Fig. 6c](#) also depicts high velocity features associated with the cratonic lithosphere. The Cheyenne Slab ([Yuan and Dueker, 2005](#)) is shown as the southern margin of the Wyoming Province. Cross-section A–A' ([Fig. 6c](#)) only shows a northward dipping southern edge to the high velocity lithosphere and does not differentiate the Cheyenne Slab from the Wyoming Province as clearly as [Yuan and Dueker \(2005\)](#). However, the cross-section B–B' ([Fig. 6d](#)) does show a thickened high velocity anomaly with an indication of a northward dip. We suggest this is the eastern end of the Cheyenne Slab, which could not be imaged by the linear array used in the CD-ROM experiment ([Yuan and Dueker, 2005](#)). [Yuan and Dueker](#)

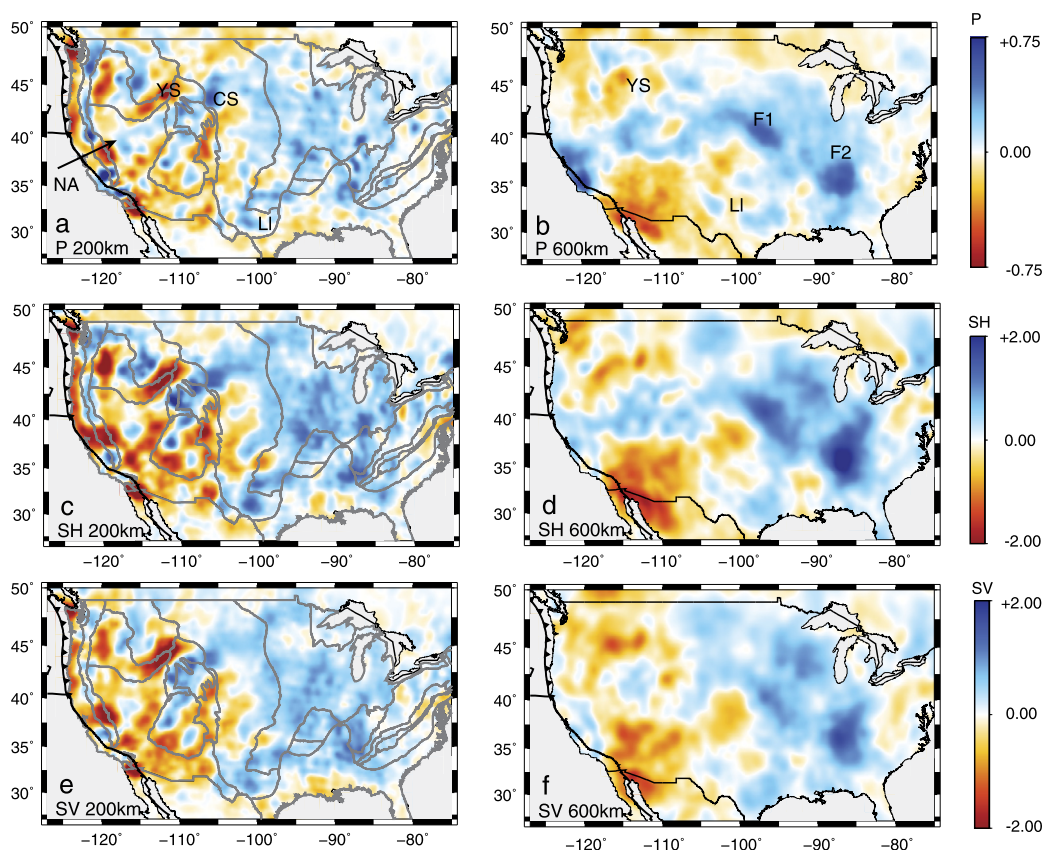


Fig. 5. Mantle maps for the 3 body-wave-only component models. Phase and depth are given in lower left corner. Maps at 200 km (a, c, and e) have the physiographic provinces from [Fenneman and Johnson \(1946\)](#) overlain in grey. Annotations given for the Yellowstone hotspot (YS), Llano Province (LI), Cheyenne Slab (CS), and Deep Farallon 1 and 2 (F1, F2).

(2005) suggest the northward dip of the Cheyenne Slab reflects a reversal of subduction polarity after back-arc closure in the Proterozoic. North of the Yellowstone Plume we image a high velocity body with similar dip and amplitude as the Cheyenne Slab, which we label the Little Belt Slab. This fossil slab is associated with the suture of the Wyoming Province with the Medicine Hat Block. The impingement of the Yellowstone plume on this fossil slab may be focusing along the old plate interface leading to the observed low velocity of the Little Belt Arc.

6.2. Llano Province

The Llano Province in Texas is shown in [Fig. 7](#). The map at 15 km ([Fig. 7a](#)) shows a primarily high velocity region with low velocities of the Gulf Coast east of the Ouachita–Marathon Front. Other low velocity anomalies in the crust are associated with the Anadarko Basin and the southern Rio Grande Rift. Immediately west of the Ouachita–Marathon Front (OMF) in Central Texas, the Llano Uplift appears as an increased high velocity anomaly. This feature represents collision of a long-lived (~50 Myr) arc being accreted to the southern margin of the Laurentia Craton from 1160–1110 Ma ([Mosher, 1998](#)).

The lower lithosphere structure presents the root of these anomalies ([Fig. 7b](#)). Low velocities are more prevalent than in the mid-crust and are primarily focused in the northwest and southeast of the region. The anomaly under the Southern Oklahoma Aulacogen separates the Llano Province from the Laurentia Craton. The Llano Province consists of an irregular high velocity body following the Grenville Front (GF), which we suggest is the Llano Slab. This slab is associated with the northeast and southwest closure events during the Mesoproterozoic. [Fig. 7c](#) highlights the south-

west portion of the Llano Slab as dipping to the north–northeast towards the Southern Oklahoma Aulacogen and Laurentia Craton. [Gao et al. \(2004\)](#) presents an alternative hypothesis after imaging the northwestern corner of this anomaly with the linear La Ristra array. They suggest the feature is a lithospheric downwelling in response to the upwelling of the Rio Grande Rift. This argument is further supported by waveform modeling of [Song and Helmberger \(2007\)](#), where the observed waveforms argue for cold and compositionally distinct mantle to 600 km depth. However, the [Gao et al. \(2004\)](#) study is limited by the array geometry and is therefore unable to capture the north–northeast dip of the feature and strike consistent with the Grenville Front. The three-dimensional geometry therefore implies a relationship to the Mesoproterozoic formation of the Llano Province.

Cross-section D–D' in [Fig. 7d](#) depicts the structure to the southeast of the Llano Uplift. This shows gradationally thicker lithosphere towards the north and a high velocity body in the mantle transition zone. Based on scattered waveform imaging by [Pavlis \(2011\)](#) showing contiguity of this feature to the northeast, we interpret this to be the southeastern portion of the Farallon plate. While most of the Farallon plate imaged under the western U.S. was north of the migrating Mendocino Triple Junction, this southern portion is associated with subduction south of the Rivera Triple Junction. The relation of the Llano Slab and southern Farallon slab is depicted in cross-section E–E' ([Fig. 7e](#)) showing that a separation is observed.

6.3. Comparison of craton constituents

The above discussion has focused on two Proterozoic provinces independently. These two provinces have several important

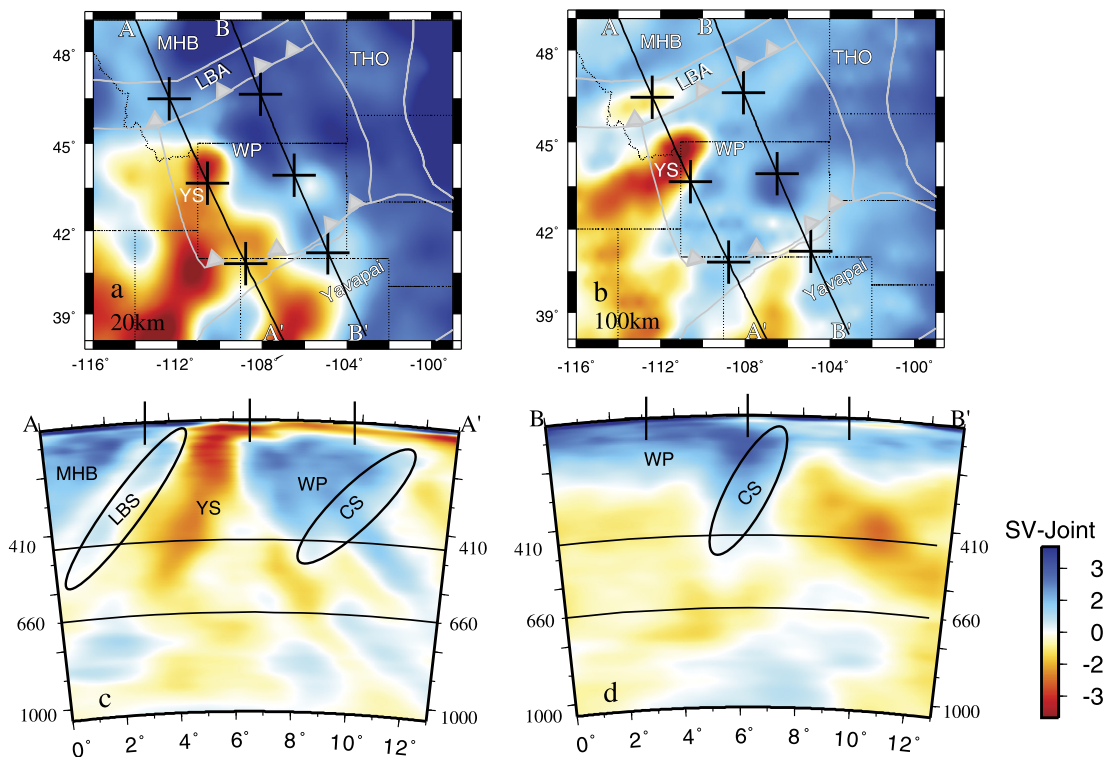


Fig. 6. Maps and cross-sections summarizing the Wyoming Province. Maps are given at (a) 20 km and (b) 100 km. Locations of profiles A–A' (c) and B–B' (d) are given on the maps. Grey lines denote province boundaries of [Whitmeier and Karlstrom \(2007\)](#). Triangles denote overriding plate in last collisional event. Annotations: Medicine Hat Block (MHB), Little Belt Arc (LBA), Little Belt Slab (LBS), Yellowstone (YS), Wyoming Province (WP), Cheyenne Slab (CS), Trans-Hudson Orogen (THO), Laurentia Craton (LC). Ovals depict approximate locations on the cross-sections.

similarities. First, we are able to identify constituent fossil slabs along some paleo-margins. The Cheyenne slab and Little Belt Slab form the southern and northern province boundaries for the Wyoming Province while the Llano Slab is at the southern boundary of the Llano province. The Cheyenne Slab and Llano Slab are associated with subduction polarity reversal as back-arc basins closed. Additionally, lithospheric low velocities are associated with preserved suture zones such as the Little Belt Arc and Southern Oklahoma Aulacogen. Based on the tectonic history of the Southern Oklahoma Aulacogen ([Keller and Stephenson, 2007](#); [Soreghan et al., 2012](#)), we suggest this is evidence of paleo-suture zones localizing deformation.

We further note some significant differences between the two provinces. The Wyoming Province had its primary orogeny to the east, via the Trans-Hudson Orogen, and no signal is seen in this suture zone: the Archean proto-continent shows no distinguishable structure relative to the eastern Laurentia Craton. However, the Llano Province has a significant zone of thinned lithosphere demarcating it from the Laurentia Craton. This is either due to variations in age of the provinces (2.0 Ga vs. 1.0 Ga) or subsequent deformation along the Southern Oklahoma Aulacogen. Additionally, in this model the Cheyenne Slab is not distinct from the Wyoming Province, but the dipping Llano Slab is a much thicker high velocity anomaly than the base of the Llano lithosphere. This suggests a significant rheological difference between the slabs, which may be a due a combination of cooling, ambient mantle conditions at time of formation, age at time of accretion, or post-accretion deformation.

These provinces are both bordered by actively upwelling features (Yellowstone and the Rio Grande Rift) and it is therefore conceivable that these high velocity anomalies are actively downwelling parts of the convection cell. The waveform modeling of [Song and Helmberger \(2007\)](#) presents a strong argument for de-

pleted lithosphere in the case of the Llano Slab. In this case, the slab formed the flat base of the Llano Province lithosphere and has since detached from the northwest due to the flow associated with the Rio Grande Rift. However, the lack of recent topographic uplift and quaternary volcanism above the proposed detachment front related to a lithospheric detachment argues against this interpretation. For the Cheyenne Slab and Little Belt Slab, any sign of detachment is less pronounced. The slabs highlighted in [Fig. 6](#) are contiguous through the lithosphere and not clearly distinct from the Archean provinces. The slabs are therefore part of the cratonic lithosphere.

6.4. Deep Farallon structure

The main feature in the model below the cratonic lithosphere is the Farallon slab. Deviations from the expected homogeneous planar structure of this feature include two high velocity anomalies (F1, F2, [Fig. 8a](#)) and significant topography of the slab surface under the Central Lowlands (CL) and Ozark Plateau (OzP) as imaged in the SV-Joint model. These anomalies may either be due to heterogeneities within the plate before it reached the trench, or they may have formed during subduction due to a combination of geometrical forcing and mineralogical phase transitions. One possible source of heterogeneity in the plate arises from a plume-ridge interaction similar to Iceland. In this scenario, a buoyant mantle plume intersects a paleo-ridge and is currently observed as the shallow portion of the Farallon slab at ~500 km depth ([Fig. 8b](#), anomaly EF). The highest velocities, F1 and F2, could be oceanic plateaus formed by this plume at the ridge and pushed apart as spreading continued. Alternatively, these anomalies may be the conjugate Hess Rise and conjugate Shatsky Rise as proposed by [Liu et al. \(2010\)](#). This scenario does not require a subducted ridge and explains the modern oceanic plateaus. The imaged high velocity anomalies are thickened piles of the stishovite

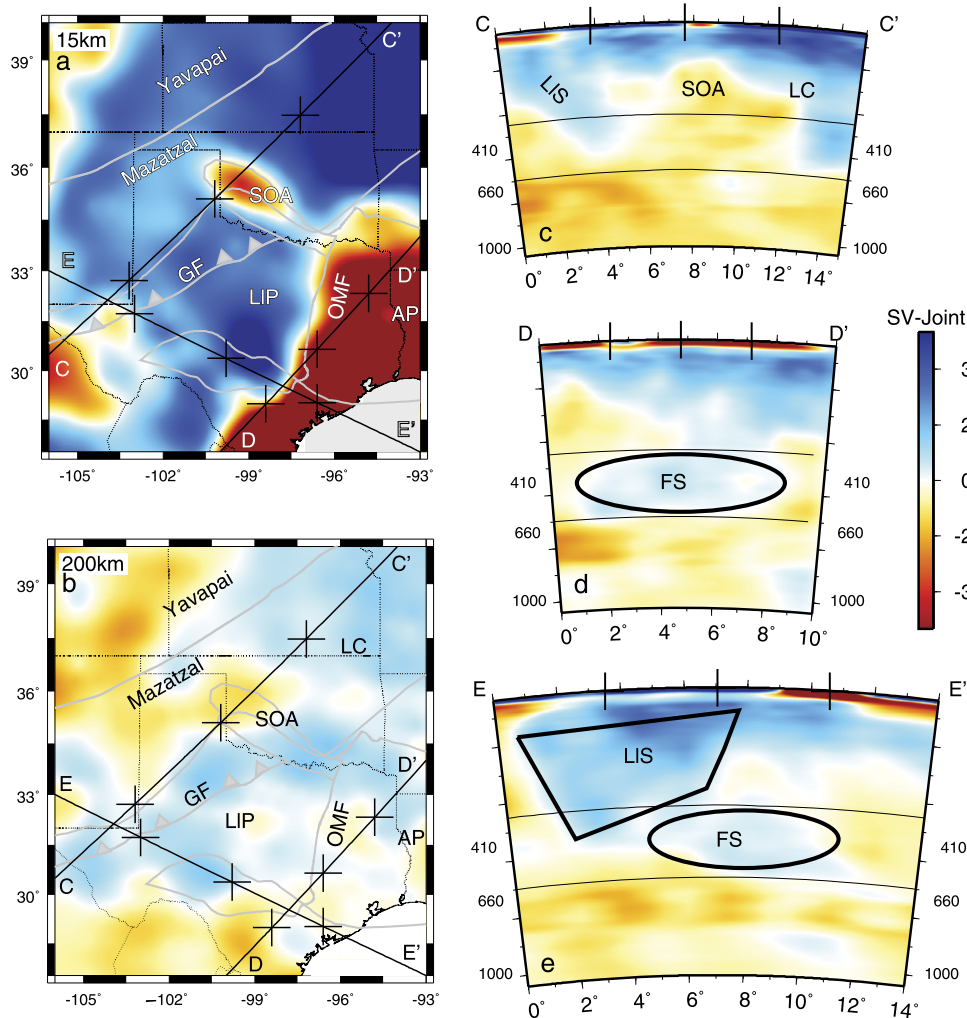


Fig. 7. Structure of the Llano Province. Maps depict structure at (a) 15 km and (b) 200 km. Also shown are the locations of profiles C–C' (c), D–D' (d), and E–E' (e). Grey lines denote province boundaries from [Whitmeyer and Karlstrom \(2007\)](#). Triangles denote overriding plate in last collisional event. Polygons overlain in (d), (e) are the interpreted Farallon slab and Llano Slab. Annotations: Laurentia Craton (LC), Ouachita–Marathon Front (OMF), Llano Province (LIP), Llano Slab (LIS), Southern Oklahoma Aulacogen (SOA), Grenville Front (GF), and Farallon Slab (FS).

component of basalt after the post-stishovite transition, which has a higher than ambient mantle seismic velocity ([Liu et al., 2010](#); [Hirose et al., 1999](#); [Carpenter et al., 2000](#)). Therefore, this thickened pile of basalt has a neutral to positive buoyancy with a positive velocity anomaly. However, this phase transition occurs as shallow as ~ 800 km ([Liu et al., 2010](#); [Hirose et al., 1999](#); [Lakshatnov et al., 2007](#)) and the imaged anomalies are as shallow as 600 km.

7. Summary

The DNA13 tomographic models illuminate the upper mantle structure beneath the contiguous U.S. These models adapt a ray-centric rotation into the P–SV–SH coordinate frame to provide multiple estimates of the velocity structure. SV constraints are also provided by Rayleigh waves, which are integrated into a joint body-wave and surface-wave inversion. Assessment of the predictive power of the models shows that we are able to predict delay times of new events to a high level of accuracy giving us confidence in the modeled structure.

We propose that imaged structures are the fossil remains of continental formation and provide insights to subduction kinematics and continental plate formation. The Wyoming Province retains evidence of fossil slabs along its southern (Cheyenne) and northern

(Little Belt) boundaries. The Yellowstone plume is impinging on its western edge. This Paleoproterozoic province has some significant differences from the Mesoproterozoic Llano Province. While both have evidence of fossil slabs, the Wyoming Province is continuous with the Laurentia Craton, while a zone of thinned lithosphere separates the Llano Province from the craton. This may either be due to the deformation localized along the Southern Oklahoma Aulacogen or variations in proterozoic mantle rheology.

The deep eastern end of the Farallon plate is imaged to be shallower than may be expected for a slab subducted in the middle Mesozoic. The higher velocity anomalies around the shallow part of the slab may suggest this is a subducted oceanic plateau formed from the intersection of a plume and a ridge. This process is analogous to modern Iceland and the thickened crustal component may provide the necessary positive buoyancy to keep the slab at a relatively shallow depth. The observed high velocity anomalies are due to the stishovite to post-stishovite component in the subducted basaltic crust.

Acknowledgements

All figures were made with Generic Mapping Tools (GMT). We'd like to thank IRIS and Earthscope for the USArray dataset. We'd like to thank Robert Smith for sharing relative delay times for the

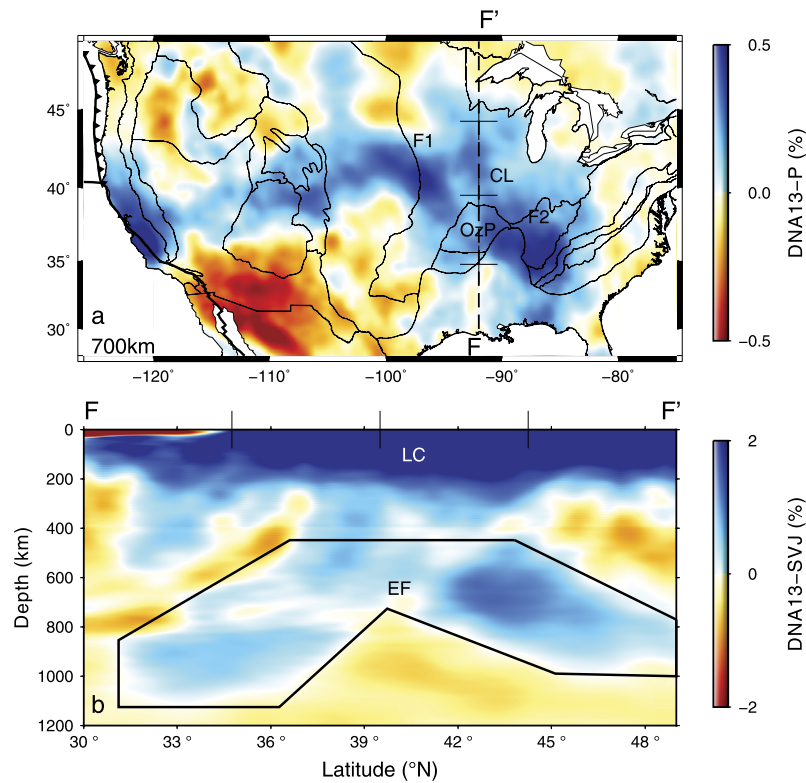


Fig. 8. Deep structure in the model. (a) Map slice through the P model at 700 km depth. (b) Longitudinal profile from south-to-north depicting the structure of the deep farallon slab. Abbreviations: Deep Farallon 1 and 2 (F1, F2), Eastern Farallon (EF), Central Lowlands (CL), Ozark Plateau (OzP), and Laurentia Craton (LC).

Yellowstone network (after Waite et al., 2006). We'd also like to thank UC Berkeley undergraduate Jenny Taing for helping derive arrival time measurements. We thank Shu-Huei Hung and Mathias Obrebski for continued use of software and the rest of the UC Berkeley regional imaging group (Cheng Cheng, William Hawley, Qingkai Kong, and Robert Martin Short) for continuing discussion on early versions of this manuscript. This manuscript was improved by comments from two anonymous reviewers. This work was funded by National Science Foundation grants EAR-0643077 and EAR-0745934.

Appendix A. Supplementary material

Supplementary material related to this article can be found online at <http://dx.doi.org/10.1016/j.epsl.2013.10.034>.

References

- Abt, D.L., Fischer, K.M., French, S.W., Ford, H.A., Yuan, H., Romanowicz, B., 2010. North American lithospheric discontinuity structure imaged by Ps and Sp receiver functions. *J. Geophys. Res.* **115** (B9), 1978–2012.
- Barmin, M.P., Ritzwoller, M.H., Levshin, A.L., 2001. A fast and reliable method for surface-wave tomography. *Pure Appl. Geophys.* **158** (8), 1351–1375.
- Becker, T.W., 2012. On recent seismic tomography for the western United States. *Geochem. Geophys. Geosyst.* **13**, Q01W10. <http://dx.doi.org/10.1029/2011GC003977>.
- Bostock, M.G., 1998. Mantle stratigraphy and evolution of the Slave province. *J. Geophys. Res.* **103** (B9), 21183–21200. <http://dx.doi.org/10.1029/98JB01069>.
- Braile, L.W., Hinze, W.J., Sexton, J.L., Keller, G.R., Lidiak, E.G., 1986. Tectonic development of the New Madrid seismic zone. *Tectonophysics* **131**, 1–21. [http://dx.doi.org/10.1016/0040-1951\(86\)90265-9](http://dx.doi.org/10.1016/0040-1951(86)90265-9).
- Burdick, S., Li, C., Martynov, V., Cox, T., Eakins, J., Mulder, T., Astiz, L., Vernon, F.L., Pavlis, G.L., van der Hilst, R.D., 2008. Upper mantle heterogeneity beneath North America from travel time tomography with global and USArray Transportable Array data. *Seismol. Res. Lett.* **79**, 384–390.
- Burdick, S., van der Hilst, R.D., Vernon, F.L., Martynov, V., Cox, T., Eakins, J., Karasu, G.H., Tylell, J., Astiz, L., Pavlis, G.L., 2012. Model update March 2011: Upper mantle heterogeneity beneath North America from traveltome tomography with global and USArray transportable array data. *Seismol. Res. Lett.* **83**, 23–28. <http://dx.doi.org/10.1785/gssrl.83.1.23>.
- Carpenter, M.A., Hemley, R.J., Mao, H.-K., 2000. High-pressure elasticity of stishovite and the P42/mnm \leftrightarrow Pnmm phase transition. *J. Geophys. Res.* **105**, 10807–10816.
- Chulick, G.S., Mooney, W.D., 2002. Seismic structure of the crust and uppermost mantle of North America and adjacent oceanic basins: a synthesis. *Bull. Seismol. Soc. Am.* **92**, 2478–2492. <http://dx.doi.org/10.1785/0120010188>.
- Crotwell, H.P., Owens, T.J., Ritsema, J., 1999. The TauP Toolkit: Flexible seismic travel-time and ray-path utilities. *Seismol. Res. Lett.* **70**, 154–160.
- Duebendorfer, E.M., Houston, R.S., 1986. Kinematic history of the Cheyenne belt, Medicine Bow Mountains, southeastern Wyoming. *Geology* **14**, 171–174.
- Fenneman, Johnson, 1946. Physiographic divisions of the conterminous U.S. USGS open map file. Accessed online September 5, 2013. <http://water.usgs.gov/GIS/metadata/usgswrd/XML/physio.xml>.
- Foster, D.A., Mueller, P.A., Mogk, D.W., Wooden, J.L., Vogl, J.L., 2006. Proterozoic evolution of the western margin of the Wyoming craton: Implications for the tectonic and magmatic evolution of the northern Rocky Mountains. *Can. J. Earth Sci.* **43**, 1601–1619. <http://dx.doi.org/10.1139/E06-052>.
- Frassetto, A.M., Zandt, G., Gilbert, H., Owens, T.J., Jones, C.H., 2011. Structure of the Sierra Nevada from receiver functions and implications for lithospheric foundering. *Geosphere* **7** (4), 898–921.
- Frederiksen, A.W., Miong, S.-K., Darbyshire, F.A., Eaton, D.W., Rondenay, S., Sol, S., 2007. Lithospheric variations across the Superior Province, Ontario, Canada: Evidence from tomography and shear wave splitting. *J. Geophys. Res.* **112**, B07318. <http://dx.doi.org/10.1029/2006JB004861>.
- Gao, W., Grand, S.P., Baldrige, W.S., Wilson, D., West, M., Ni, J., Aster, R., 2004. Upper mantle convection beneath the central Rio Grande rift by P and S wave tomography. *J. Geophys. Res.* **109**, B03305. <http://dx.doi.org/10.1029/2003JB002743>.
- Grand, S.P., 1994. Mantle shear structure beneath the Americas and surrounding oceans. *J. Geophys. Res.* **99**, 11591–11621. <http://dx.doi.org/10.1029/94JB00042>.
- van der Hilst, R.D., Widyantoro, S., Engdahl, E.R., 1997. Evidence for deep mantle circulation from global tomography. *Nature* **386**, 578–584.
- Hirose, K., Fei, Y., Ma, Y., Mao, H.-K., 1999. The fate of subducted basaltic crust in the Earth's lower mantle. *Nature* **397**, 53–56.
- Hoffman, P.F., 1988. United plates of America, the birth of a craton; early Proterozoic assembly and growth of Laurentia. *Annu. Rev. Earth Planet. Sci.* **16**, 543–603. <http://dx.doi.org/10.1146/annurev.ea.16.050188.002551>.
- Humphreys, E., Hessler, E., Dueker, K., Erslev, E., Farmer, G.L., Atwater, T., 2003. How Laramide-age hydration of North America by the Farallon slab controlled subsequent activity in the western U.S. *Int. Geol. Rev.* **45**, 575–595. <http://dx.doi.org/10.2747/0020-6814.45.7.575>.

- Hung, S.H., Dahlen, F.A., Nolet, G., 2000. Fréchet kernels for finite-frequency travel-times – II. Examples. *Geophys. J. Int.* 141, 175–203.
- James, D.E., Fouch, M.J., Carlson, R.W., Roth, J.B., 2011. Slab fragmentation, edge flow and the origin of the Yellowstone hotspot track. *Earth Planet. Sci. Lett.* 311, 124–135. <http://dx.doi.org/10.1016/j.epsl.2011.09.007>.
- Julia, J., Ammon, C.J., Herrmann, R.B., Correig, A.M., 2000. Joint in-version of receiver function and surface wave dispersion observations. *Geophys. J. Int.* 143, 99–112.
- Keller, G.R., Stephenson, R.A., 2007. The southern Oklahoma and Dnieper–Donets aulacogens: A comparative analysis. 4-D framework of continental crust. *Geol. Soc. Am. Memoir* 200, 127–143. [http://dx.doi.org/10.1130/2007.1200\(08\)](http://dx.doi.org/10.1130/2007.1200(08)).
- Kennett, B.L.N., Engdahl, E.R., 1991. Travel times for global earthquake location and phase association. *Geophys. J. Int.* 105, 429–465.
- Lakshatanov, D.L., Sinogeikin, S.V., Litasov, K.D., Prakupenka, V.B., Hellwig, H., Wang, J., Sanches-Vale, C., Perrillat, J.-P., Chen, B., Somayazulu, M., Li, J., Ohtani, E., Bass, J.D., 2007. The post-stishovite phase transition in hydrous alumina-bearing SiO₂ in the lower mantle of the earth. *Proc. Natl. Acad. Sci. USA* 104, 13588–13590.
- Lee, C.-T.A., 2006. Geochemical/petrologic constraints on the origin of cratonic mantle. In: Benn, K., Mareschal, J.-C., Condie, K.C. (Eds.), *Archean Geodynamics and Environments*. In: *Geophys. Monogr.*, vol. 164. AGU, Washington, DC, pp. 89–114.
- van der Lee, S., Nolet, G., 1997. Seismic image of the subducting trailing fragments of the Farallon plate. *Nature* 386, 266–269. <http://dx.doi.org/10.1038/386266a0>.
- Liu, L., Gurnis, M., Seton, M., Saleeby, J., Müller, R.D., Jackson, J.M., 2010. The role of oceanic plateau subduction in the Laramide orogeny. *Nat. Geosci.* 3, 353–357. <http://dx.doi.org/10.1038/NGeo0829>.
- Liu, K., Levander, A., Niu, F., Miller, M.S., 2011. Imaging crustal and upper mantle structure beneath the Colorado Plateau using finite frequency Rayleigh wave tomography. *Geochem. Geophys. Geosyst.* 12, Q07001. <http://dx.doi.org/10.1029/2011GC003611>.
- Liu, K., Levander, A., Zhai, Y., Porritt, R.W., Allen, R.M., 2012. Asthenospheric flow and lithospheric evolution near the Mendocino Triple Junction. *Earth Planet. Sci. Lett.* 323, 60–71. <http://dx.doi.org/10.1016/j.epsl.2012.01.020>.
- Mosher, S., 1998. Tectonic evolution of the southern Laurentian Grenville orogenic belt. *Geol. Soc. Am. Bull.* 110, 1357–1375.
- Mueller, P.A., Heatherington, A.L., Kelly, D.M., Wooden, J.L., Mogk, D.W., 2002. Paleoproterozoic crust within the Great Falls tectonic zone: Implications for the assembly of southern Laurentia. *Geology* 30, 127–130. [http://dx.doi.org/10.1130/0091-7613\(2002\)030<0127:PCWTGF>2.0.CO;2](http://dx.doi.org/10.1130/0091-7613(2002)030<0127:PCWTGF>2.0.CO;2).
- Nicholson, C., Sorlien, C.C., Atwater, T., Crowell, J.C., Luyendyk, B.P., 1994. Microplate capture, rotation of the western Transverse Ranges, and initiation of the San Andreas transform as a low-angle fault system. *Geology* 22, 491–495.
- Obrebski, M., Allen, R.M., Xue, M., Hung, S.-H., 2010. Slab–plume interaction beneath the Pacific Northwest. *Geophys. Res. Lett.* 37, L14305. <http://dx.doi.org/10.1029/2010GL043489>.
- Obrebski, M., Allen, R.M., Pollitz, F., Hung, S.-H., 2011. Lithosphere–asthenosphere interaction beneath the western United States from the joint inversion of body-wave traveltimes and surface-wave phase velocities. *Geophys. J. Int.* 185, 1003–1021. <http://dx.doi.org/10.1111/j.1365-246X.2011.04990.x>.
- Pavlis, G.L., 2011. Three-dimensional wavefield imaging of data from the USArray: New constraints on the geometry of the Farallon slab. *Geosphere* 7, 785–801.
- Pavlis, G.L., Sigloch, K., Burdick, S., Fouch, M.J., Vernon, F., 2012. Unraveling the geometry of the Farallon Plate: Synthesis of three-dimensional imaging results from the USArray. *Tectonics* 31, 525–535, 82–102. <http://dx.doi.org/10.1016/j.tecto.2012.02.008>.
- Pikser, J.E., Forsyth, D.W., Hirth, G., 2012. Along-strike translation of a fossil slab. *Earth Planet. Sci. Lett.* 331–332, 315–321.
- Pollitz, F.F., Snoke, J.A., 2010. Rayleigh-wave phase-velocity maps and three-dimensional shear velocity structure of the western US from local non-plane surface wave tomography. *Geophys. J. Int.* 180, 1153–1169. <http://dx.doi.org/10.1111/j.1365-246X.2009.04441.x>.
- Porritt, R.W., Allen, R.M., Boyarko, D.C., Brudzinski, M.R., 2011. Investigation of Cascadia Segmentation with Ambient Noise Tomography. *Earth Planet. Sci. Lett.* 185, 67–76. <http://dx.doi.org/10.1016/j.epsl.2011.06.026>.
- Roscoe, S.M., Card, K.D., 1993. The reappearance of the Huronian in Wyoming: Rifting and drifting of ancient continents. *Can. J. Earth Sci.* 30, 2475–2480.
- Ross, G.M., 2002. Evolution of Precambrian continental lithosphere in western Canada: Results from Litho-probe studies in Alberta and beyond. *Can. J. Earth Sci.* 39, 413–437. <http://dx.doi.org/10.1139/e02-012>.
- Schellart, W.P., Stegman, D.R., Farrington, R.J., Freeman, J., Moresi, L., 2010. Cenozoic Tectonics of Western North America Controlled by Evolving Width of the Farallon Slab. *Science* 329, 316–319. <http://dx.doi.org/10.1126/science.1190366>.
- Schmandt, B., Humphreys, E., 2010. Complex subduction and small-scale convection revealed by body-wave tomography of the western United States upper mantle. *Earth Planet. Sci. Lett.* 297, 435–445. <http://dx.doi.org/10.1016/j.epsl.2010.06.047>.
- Schmandt, B., Dueker, K., Humphreys, E., Hansen, S., 2012. Hot mantle upwelling across the 660 beneath Yellowstone. *Earth Planet. Sci. Lett.* 331–332, 224–236. <http://dx.doi.org/10.1016/j.epsl.2012.03.025>.
- Sigloch, K., 2011. Mantle provinces under North America from multifrequency P wave tomography. *Geochem. Geophys. Geosyst.* 12, Q02W08. <http://dx.doi.org/10.1029/2010GC003421>.
- Sine, C.R., Gao, W., Grand, S.P., Aster, R., Ni, J., Baldrige, W.S., 2008. Mantle structure beneath the western edge of the Colorado Plateau. *Geophys. Res. Lett.* 35, L10303. <http://dx.doi.org/10.1029/2008GL033391>.
- Snyder, D.B., 2008. Stacked uppermost mantle layers within the Slave craton of NW Canada as defined by anisotropic seismic discontinuities. *Tectonics* 27, TC4006. <http://dx.doi.org/10.1029/2007TC002132>.
- Song, T.-R.A., Helmberger, D.V., 2007. P and S waveform modeling of continental sub-lithospheric detachment at the eastern edge of the Rio Grande Rift. *J. Geophys. Res.* 112, B07319. <http://dx.doi.org/10.1029/2007JB004942>.
- Soreghan, G.S., Keller, G.R., Gilbert, C.M., Chase, C.G., Sweet, D.E., 2012. Load-induced subsidence of the Ancestral Rocky Mountains recorded by preservation of Permian landscapes. *Geosphere*, published online <http://dx.doi.org/10.1130/GES00681.1>.
- Thomas, W.A., Astini, R.A., 1999. Simple-shear conjugate rift margins of the Argentine Precordillera and the Ouachita embayment of Laurentia. *Geol. Soc. Am. Bull.* 111, 1069–1079. <http://dx.doi.org/10.1130/0016-7606.111<1069:SS-CRMO>2.3.CO;2>.
- Tian, Y., Zhou, Y., Sigloch, K., Nolet, G., Laske, G., 2011. Structure of North American mantle constrained by simultaneous inversion of multiple-frequency SH, SS, and Love waves. *J. Geophys. Res.* 116, B02307. <http://dx.doi.org/10.1029/2010JB007704>.
- Tromp, J., Komatitsch, D., Hjørleifsdóttir, V., Liu, Q., Zhu, H., Peter, D., Bozdog, E., McRitchie, D., Friberg, P., Trabant, C., Hutko, A., 2010. Near real-time simulations of global CMT earthquakes. *Geophys. J. Int.* 183, 381–389. <http://dx.doi.org/10.1111/j.1365-246X.2010.04734.x>.
- VanDecar, J.C., Crosson, R.S., 1990. Determination of teleseismic relative phase arrival times using multi-channel cross-correlation and least squares. *Bull. Seismol. Soc. Am.* 80, 150–169.
- Van Schmus, W.R., Hinze, W.J., 1985. The midcontinent rift system. *Annu. Rev. Earth Planet. Sci.* 13, 345–383.
- Villeneuve, M.E., Ross, G.M., Theriault, R.J., Milews, W., Parrish, R.R., Broome, J., 1993. Tectonic subdivision and U–Pb geochronology of the crystalline basement of the Alberta Basin, western Canada. *Bull. Geol. Surv. Can.* 447, 1–25.
- Waite, G.P., Smith, R.B., Allen, R.M., 2006. VP and VS structure of the Yellowstone hot spot from teleseismic tomography: evidence for an upper mantle plume. *J. Geophys. Res.* 111, B04303. <http://dx.doi.org/10.1029/2005JB003867>.
- Wang, Y., Forsyth, D.W., Rau, C.J., Carriero, N., Schmandt, B., Gaherty, J., Savage, B., 2013. Fossil slabs attached to unsubducted fragments of the Farallon Plate. *Proc. Natl. Acad. Sci. USA* 110 (14), 5342–5346.
- Whitney, S.J., Karlstrom, K.E., 2007. Tectonic model for the Proterozoic growth of North America. *Geosphere* 3 (4), 220–259. <http://dx.doi.org/10.1130/GES00055.1>.
- Xue, M., Allen, R.M., 2007. The Fate of the Juan de Fuca Plate: Implications for a Yellowstone Plume Head. *Earth Planet. Sci. Lett.* 264, p266–276. <http://dx.doi.org/10.1016/j.epsl.2007.09.047>.
- Xue, M., Allen, R.M., 2010. Mantle structure beneath the western US and its implications for convection processes. *J. Geophys. Res.* 115, B07303. <http://dx.doi.org/10.1029/2008JB006079>.
- Yang, Y., Ritzwoller, M.H., Lin, F.-C., Moschetti, M.P., Shapiro, N.M., 2008. The structure of the crust and uppermost mantle beneath the western US revealed by ambient noise and earthquake tomography. *J. Geophys. Res.* 113, B12310.
- Yuan, H., Dueker, K., 2005. Upper mantle tomographic Vp and Vs images of the Rocky Mountains in Wyoming, Colorado and New Mexico: Evidence for a thick heterogeneous chemical lithosphere. *Geophys. Monogr.*, vol. 154, pp. 329–345.
- Yuan, Romanowicz B. H., Fischer, K.M., Abt, D., 2011. 3-D shear wave radially and azimuthally anisotropic velocity model of the North American upper mantle. *Geophys. J. Int.* 184 (3), 1237–1260.
- Zandt, G., Gilbert, H., Owens, T.J., Duca, M., Saleeby, J., Jones, C.H., 2004. Active founding of a continental arc root beneath the southern Sierra Nevada in California. *Nature* 431, 41–46.